Al-Azhar Bulletin of Science

Volume 34 | Issue 1 Article 2

4-2023
Section: Earth science

# Geological mapping using remote sensing, GIS, field studies and laboratory data of Wadi Hammamat area, Central Eastern Desert, Egypt

Moamen M. Badr
*Geology department, Faculty of science, Al-Azhar University, Nasr City, Cairo, Egypt*,
momenbadr@azhar.edu.eg

Ahmed M. El Mezayen
*Geology department, Faculty of science, Al-Azhar University, Nasr City, Cairo, Egypt*

S. M. Salem
*Geology department, National Authority for Remote Sensing and Space Sciences, Cairo, Egypt*

Sherif A. Taalab
*Geology department, Faculty of science, Al-Azhar University, Nasr City, Cairo, Egypt*

Follow this and additional works at: https://absb.researchcommons.org/journal

 Part of the Remote Sensing Commons

## How to Cite This Article

Badr, Moamen M.; Mezayen, Ahmed M. El; Salem, S. M.; and Taalab, Sherif A. (2023) "Geological mapping using remote sensing, GIS, field studies and laboratory data of Wadi Hammamat area, Central Eastern Desert, Egypt," *Al-Azhar Bulletin of Science*: Vol. 34: Iss. 1, Article 2.
DOI: https://doi.org/10.58675/2636-3305.1636

This Original Article is brought to you for free and open access by Al-Azhar Bulletin of Science. It has been accepted for inclusion in Al-Azhar Bulletin of Science by an authorized editor of Al-Azhar Bulletin of Science. For more information, please contact kh_Mekheimer@azhar.edu.eg.

ORIGINAL ARTICLE

# Geological Mapping Using Remote Sensing, GIS, Field Studies and Laboratory Data of Wadi Hammamat Area, Central Eastern Desert, Egypt

Moamen Mohammed Badr [a,*], Ahmed Mohammed El Mezayen [a], Salem Mohammed Salem [b], Sherif Abd El Aziz Taalab [a]

[a] Geology Department, Faculty of Science, Al-Azhar University, Nasr City, Cairo, Egypt
[b] Geology Department, National Authority for Remote Sensing and Space Sciences, Cairo, Egypt

**Abstract**

**In the present study, the Operational Land Imager (OLI) images have been used with several processing approaches for delineating the different rock units of the Wadi Hammamat area. To validate the remote sensing data, a geological map of the Wadi Hammamat area at a scale of 1:20 000 was produced using a Geographic Information System (GIS) and field research. The geological map of the research area has been improved and modified using several a variety of image processing methods, such as False color composite (FCC), Principal Component Analysis (PCA), Minimum Noise Fraction (MNF), and Band Ratio (BR). The best band combination of FCC 761 762 and 751 RGB. The result of PCA is PCA1, PCA2 and PCA3 show well lithological differentiation, while the best result of PCA is PC5, PC2, and PC3. In which it can distinguish between the different types of Hammamat molasse sediments; Hammamat graywacke, Hammamat siltstone, and Hammamat conglomerate. A new proposed FCC band ratio (7/5, 5/3&3/1) has been developed as a best lithological discrimination.**

*Keywords:* Band ratio, Landsat 8, Operational land imager, Wadi hammamat

## 1. Introduction

The study area lies in the Central Eastern Desert as a part of the Arabian Nubian Shield (ANS) which has been formed during the Neoproterozoic Era (1000−540 Ma) and affected by East African Orogeny (EAO). This shield covers most of northeast Africa and the Arabian Peninsula, with a total area of about 3 million km$^2$. It was a stable continental crust by early Cambrian at 530 Ma, including tectonic and magmatic events operated during the Neoproterozoic rocks and resulted in the breakup of Rodina and formation of Gondwana [1−6]. The Central Eastern Desert represents a complete succession of the Neoproterozoic basement encountered elsewhere in the ANS. Several attempts have been made to classify and categorize these rocks [7−18]. The Central Eastern Desert (CED) is affected by two distinguished tectonostratigraphic units; infrastructure [19] and suprastructure [19,20], the infrastructure is the lower unit comprises a high grade of metamorphic gneisses and migmatites, schists, and amphibolite.

Remote sensing techniques have been developed by many authors to contribute to the geological mapping of different geological regions [21−27]. Satellite images help to identify the topography of the earth's surface, agricultural areas, and environmental changes. The image processing of the Satellite image is efficient in the geological features such as, lithological discrimination, mineral and alteration zones mapping.

## 2. Geologic setting

Wadi Hammamat area is situated along the Qift - Quseir road, bounded by latitudes 26° 6′ 27″, 25° 57′

Received 23 November 2022; revised 11 December 2022; accepted 23 December 2022.
Available online 18 August 2023

* Corresponding author at: Geology Department, Faculty of Science, Al-Azhar University, P.O. Box 11884, Nasr City, Cairo, Egypt.
E-mail address: momenbadr@azhar.edu.eg (Moamen. M. Badr).

https://doi.org/10.58675/2636-3305.1636
2636-3305/© 2023, The Authors. Published by Al-Azhar university, Faculty of science. This is an open access article under the CC BY-NC-ND 4.0 Licence (https://creativecommons.org/licenses/by-nc-nd/4.0/).

7″ N and longitudes 33° 25′ 5″, 33° 37′ 19″ E, covering about 7200 km$^2$ (Fig. 1). The study area includes low-grade metamorphosed dismembered ophiolite sections such as serpentinites, pillow lavas and arc metavolcanic. These units were intruded by calc-alkaline granites and diorite [28]. During the later stage of crustal growth of the CED, the eruption of the Dokhan volcanics and the deposition of Hammamat molasse sediments have been formed (Table 1). The serpentinites are described as light green to dark brown color, found as rugged peaks in the Bir Um Fawakhir area and associated by talc-carbonates, they are also found at Wadi Atalla as dismembered ophiolite and mélange overthrusted the metavolcanics. Pillowed Basalts exposed in the northwest of the upper part of Wadi Atalla at Wadi Um Seleimat, mainly associated with acid to intermediate metavolcanics and intruded by the monzogranite with sharp intrusive contact. The metavolcanic outcrop pervades Bir Um Fawakhir and Wadi Atalla in the study area, and is described as fine to very fine grained, greyish green to dark grey in color. The older granitoids are present in the northern part of G. Um Had and Wadi El Sid at the southern part of the Bir Um Fawakhir area, mainly as blocks and boulders due to weathering. They are intruded by the younger phase of monzogranite rocks. Hammamat molasse sediments are deposited

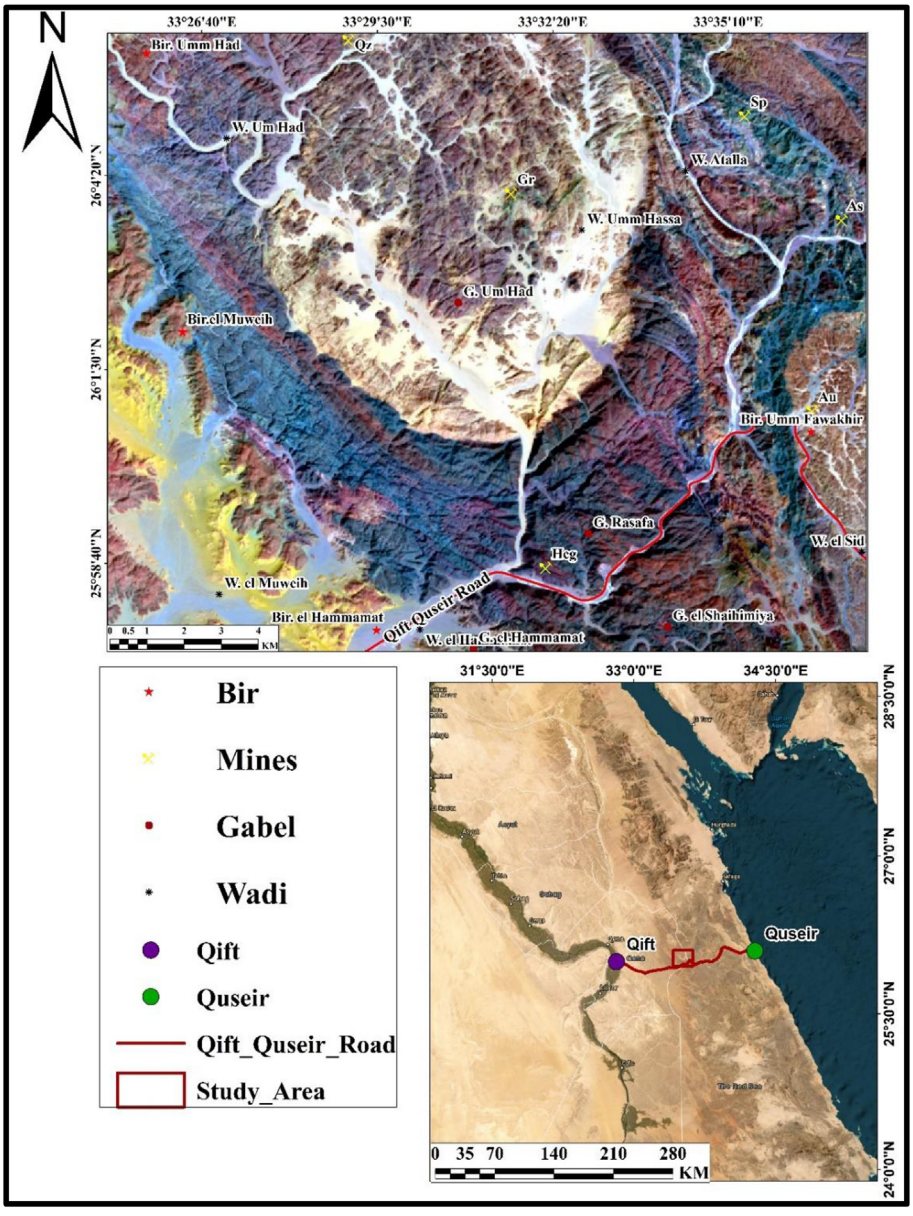


*Fig. 1. Location map of the study area.*

*Table 1. The rocks that the area contains and their symbols.*

| No. | Name | | Symbols | |
|---|---|---|---|---|
| 7 | Wadi deposits | | WD | Youngest |
| 6 | Nubia Sandstone | | NS | |
| | Younger granitoids | Alkali granite | AG | |
| | | Monzogranite | MG | |
| 4 | Hammamat molasses sediments | Graywackes | HGW | |
| | | Conglomerate | HC | |
| | | Silt | HS | |
| 3 | Island arc | Tonalite granodiorite | TG | |
| | | Acid to intermediate metavolcanics | AMV | |
| | | Basic to intermediate metavolcanics | BMV | |
| 2 | Dismembered ophiolitic rocks | Pillowed basalt | PB | |
| | | Serpentinite | SER | |
| 1 | Psammitic gneiss and migmatites | | PG | Oldest |

in their type locality Wadi Hammamat area, they are represented by the Shihmiya Formation, which is subdivided into three members; Rasafa siltstone, Um Had conglomerate, and Um Hassa graywacke [11]. Monzogranites are related to younger granitoids as referred by [29], they outcrop in the central part of Um Had and Bir Um Fawakhir areas, as pale pinkish massive and blocky rocks. The alkali granites outcrop in the southern part of Um Had area, intruding the Hammamat molasse sediments. The Phanerozoic Nubia sandstones rocks cover the western part of the study area.

## 3. Data and methods

This study utilized the Landsat-8 (OLI) image to distinguish between different rock units of the study area according to their spectral reflectance using various remote sensing processing techniques such as FCC, PCA, MNF, PCA and Band ratio (BR). Most remote sensing satellite images operate within the optical spectrum, which ranges from about 0.3 to 14 μm. The Landsat-8 carries two instruments, the Operational Land Imager (OLI) and the Thermal Infrared Sensor (TIRS). In this work, only VNIR and SWIR bands with 30 m spatial resolution were employed the panchromatic band 8 with 15 m spatial resolution (Table 2). Level 1 Terrain corrected (L1T) Landsat-8 images were obtained from the US Geological Survey website (https://earthexplorer.usgs.gov/). On September 25, 2020, an OLI image covering the study area was in path 174/24 row. The Landsat-8 image is projected using the UTM (Universal Transverse Mercator), Zone N36, which is related to the WGS-84 datum. Furthermore, a geological field check was conducted to validate the remote sensing results of the different rock units in the study area.

*Table 2. Landsat-8 band designations for the Operational Land Imager (OLI) and Thermal Infrared Sensor (TIRS).*

| Landsat-8 OLI and TIRS Bands (μ-m) | | |
|---|---|---|
| Bands | Wavelengths (μ-m) | Resolution (m) |
| Band 1 | 0.435–0.451 | 30 m Coastal/Aerosol |
| Band 2 | 0.452–0.512 | 30 m Blue |
| Band 3 | 0.533–0.590 | 30 m Green |
| Band 4 | 0.636–0.673 | 30 m Red |
| Band 5 | 0.851–0.879 | 30 m NIR |
| Band 6 | 1.566–1.651 | 30 m SWIR-l |
| Band 7 | 2.107–2.294 | 30 m SWIR-2 |
| Band 8 | 0.503–0.676 | 15 m Pan |
| Band 9 | 1.363–1.384 | 30 m Cirrus |
| Band 10 | 10.60–11.19 | 100 m TIR-1 |
| Band 11 | 11.50–12.51 | 100 m TIR-2 |

### 3.1. Preprocessing data

The preprocessing steps were used with OLI data to remove the atmospheric, solar, and topographic effects. The first step is radiometric calibration, which is used to calibrate data to radiance or Top of the Atmosphere (TOA) reflectance. The TOA put into account the earth–sun relationship, time of day, and year. The second algorithm is the Fast Line-of-sight Atmospheric Analysis of Spectral Hypercube (FLAASH), which is applied to radiometric calibration radiance information with the band interleaved using line (BIL) format. In the TIR bands the thermal

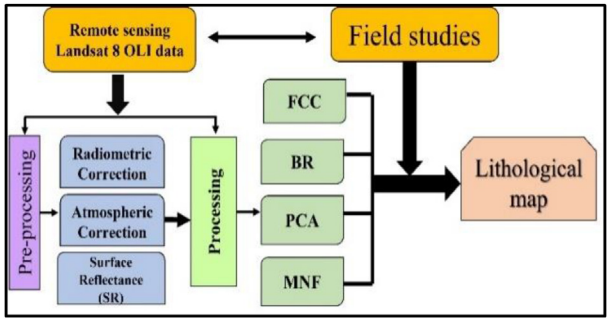


*Fig. 2. Simplified flow chart summarizes the proposed image processing scheme for the remote sensing data.*

atmospheric correction and emissivity normalization parameters have been implemented [30].

### 3.2. Processing data and methodology

Several processing techniques were applied on the OLI data for lithological mapping, such as False Color Composite (FCC), band ratio (BR), Principal Component Analysis (PCA), and Minimum Noise Fraction (MNF). Data preprocessing and processing techniques were constructed using the Environment for Visualizing Images (ENVI) 5.1, and Arc GIS 10.4, as shown in the flow chart (Fig. 2).

#### 3.2.1. Fales color composite (FCC)

Seven VNIR and SWIR spectral bands are included in the Landsat-8 (OLI) data. Only three bands are needed in a band combination to create a color image using the data from these bands. To obtain the best FCC images displaying the best lithological discrimination in the study region, several spectral bands of the OLI data were tested, chosen, and combined in RGB color composite with the Optimum Index Factor (OIF) technique using the ILWIS software (Table 3). The best band triplets are (7,6,1), (7,6,2), and (7,5,1) in RGB showing well discrimination between different rock units of the investigated area (Fig. 3).

*Table 3. OIF ranking of Landsat-8 data in the study area.*

| Rank | Band triplet | OIF % |
|---|---|---|
| 1 | 7,6,1 | 78.04 |
| 2 | 7,6,2 | 76.61 |
| 3 | 7,5,1 | 76.25 |
| 4 | 6,5,1 | 76.04 |
| 5 | 7,2,1 | 75.26 |
| 6 | 6,2,1 | 75.19 |

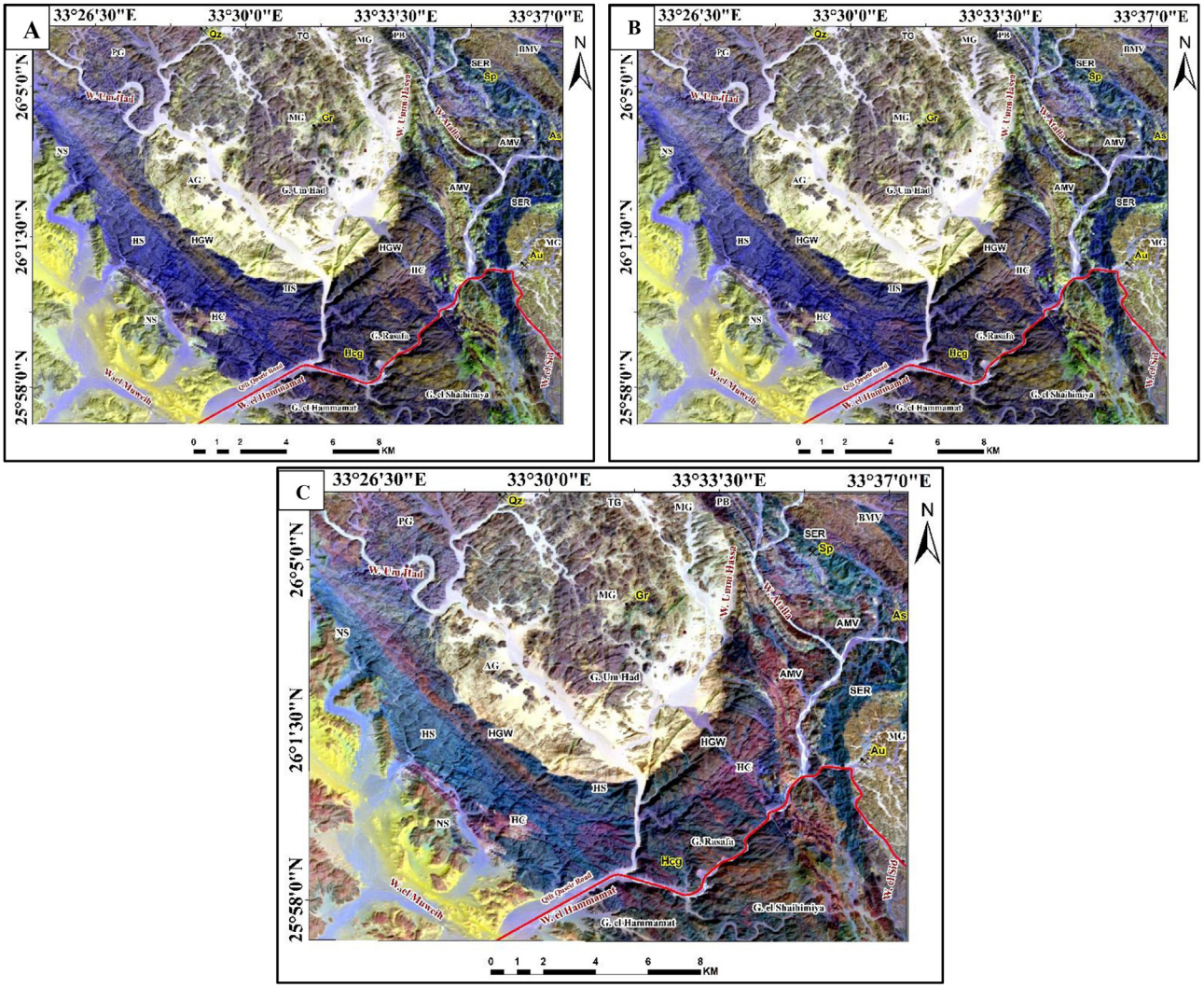


*Fig. 3. Landsat-8 FCC using OIF: (A) Landsat-8 (7,6,1) Color Combination image in (RGB). (B) Landsat-8 (7,6,2) Color Combination image in (RGB). (C) Landsat-8 (7,5,1) Color Combination image in (RGB) whereas symbols as the following: TG, Tonalite granodiorite; AMV, Acid to intermediate metavolcanics; BMV, Basic to intermediate metavolcanics; PB, Pillowed basalt; SER, Serpentinite; PG, Psammitic gneiss and migmatites; NS, Nubia sandstone; AG, Alkali granite; MG, Monzogranite; HGW, Hammamat graywackes; HC, Hammamat conglomerate; HS, Hammamat silt; Au, Gold mine; Gr, Granite mine; As, Asbestos mine; Qz, Quartz mine; Hcg, Hammamat conglomerate mine; ——, Qift_Quseir_Road; ▪, Gabel; ●, Wadi.*

### 3.2.2. Band ratio (BR)

Band-rationing is a popular and effective image processing technique that enhances spectral differences between bands and highlights anomalies by dividing one spectral band by another [31]. Ratio images are mathematical transformations for enhancements resulting from the division of DN values in one spectral band represent brightness values at peaks/maxima by the corresponding values in another band represent darkness at troughs/minima in the reflectance curve [32]. In this study, the band ratio image of three OLI-band ratios (6/7 in red (R), 6/5 in green (G), 4/2 in blue (B)) of [30] was used to differentiate the Hammamat sediments to the varied members of graywackes, conglomerate and silt. The result of such ratios displayed Hammamat graywackes and Hammamat conglomerate in green color at the southwestern side, while the silt member in maroon color at the southwestern side. Moreover, the alkali granite shows slate gray color, monzogranite dark green color, acid to intermediate metavolcanics lawn green, basic to intermediate metavolcanics dark forest green and serpentinite in tomato color (Fig. 4a). A new OLI-band ratio (7/5, 5/3 & 3/1) has been created by the author to discriminate the three Hammamat members in which the graywackes show orange color, the conglomerate red, the silt in green color. Also, the serpentinite displayed bluish green, alkali granite plum, monzogranite bale blue, acid to intermediate metavolcanics in pinkish red and basic to intermediate metavolcanics yellow violet color (Fig. 4b).

### 3.2.3. Principal component analysis (PCA)

Principal Component Analysis is a multivariate statistical method that used to reduce data redundancy by transforming the original data into new orthogonal principal component axes producing an uncorrelated image, it has significantly more contrast than the original bands [31]. PCA enables the computation of redundant data into fewer bands. The PCA bands data are non-correlated and independent and are often more interpretable than the source data [32]. The PCA statistics revealed the highest eigenvector values in Table 4. It is shown

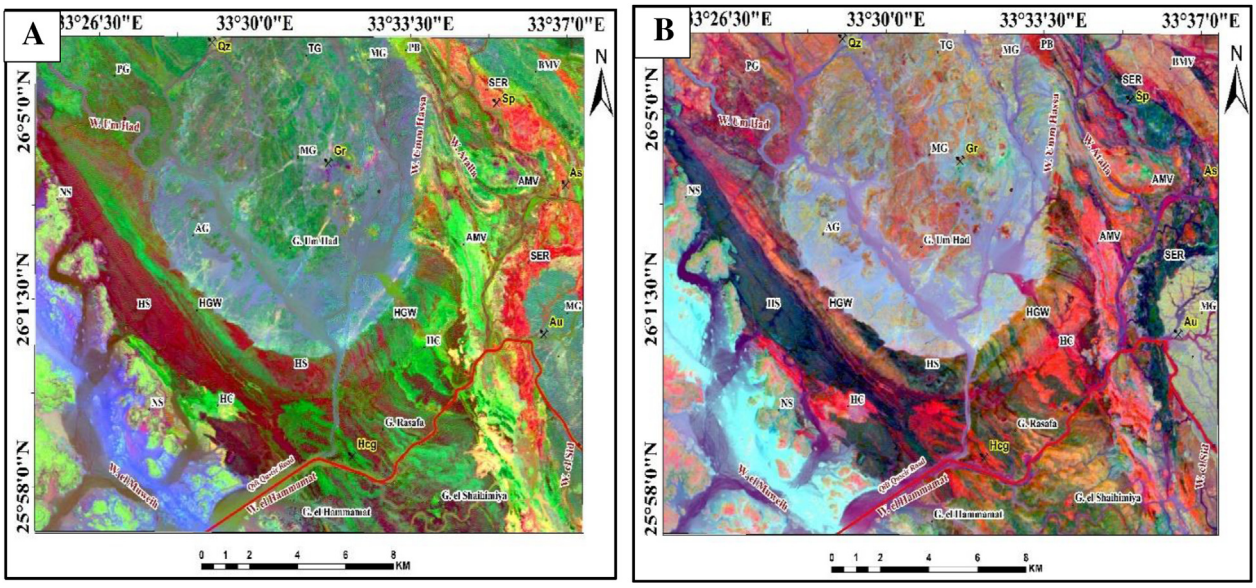


*Fig. 4. (a) FCC band ratio (6/7, 6/5 & 4/2) in RGB after (Zoheir et al., 2019). (b) FCC band ratio (7/5, 5/3&3/1) in RGB, symbols as in (Fig. 3).*

*Table 4. The eigenvector values of PCA for OLI bands and the highest eigenvector values for each band.*

| | PC1 | PC2 | PC3 | PC4 | PC5 | PC6 | PC7 |
|---|---|---|---|---|---|---|---|
| B1 | −0.90095 | −0.43104 | −0.002273 | 0.042844 | −0.011776 | −0.002221 | −0.022773 |
| B2 | 0.380049 | −0.77983 | −0.481119 | 0.052884 | −0.063372 | −0.02434 | −0.092417 |
| B3 | 0.195733 | −0.39336 | 0.857806 | 0.059904 | −0.198575 | −0.015945 | −0.16689 |
| B4 | −0.00371 | −0.09298 | 0.03135 | −0.993165 | −0.022998 | 0.04007 | 0.042976 |
| B5 | −0.04763 | 0.120294 | −0.13103 | 0.013049 | −0.971293 | −0.016729 | 0.149099 |
| B6 | 0.053372 | −0.15961 | 0.118573 | 0.049279 | 0.111673 | −0.193194 | 0.951522 |
| B7 | −0.02046 | 0.052398 | −0.021886 | −0.052953 | −0.001564 | −0.979729 | −0.183524 |
| Eigenvector | 0.02229 | 0.001061 | 0.00019 | 0.000086 | 0.000011 | 0 | 0 |
| Eigenvector | 0.942973 | 0.044885 | 0.0080379 | 0.0036382 | 0.00046535 | 0 | 0 |
| % | 94.29732 | 4.488535 | 0.8037905 | 0.363821 | 0.04653524 | 0 | 0 |

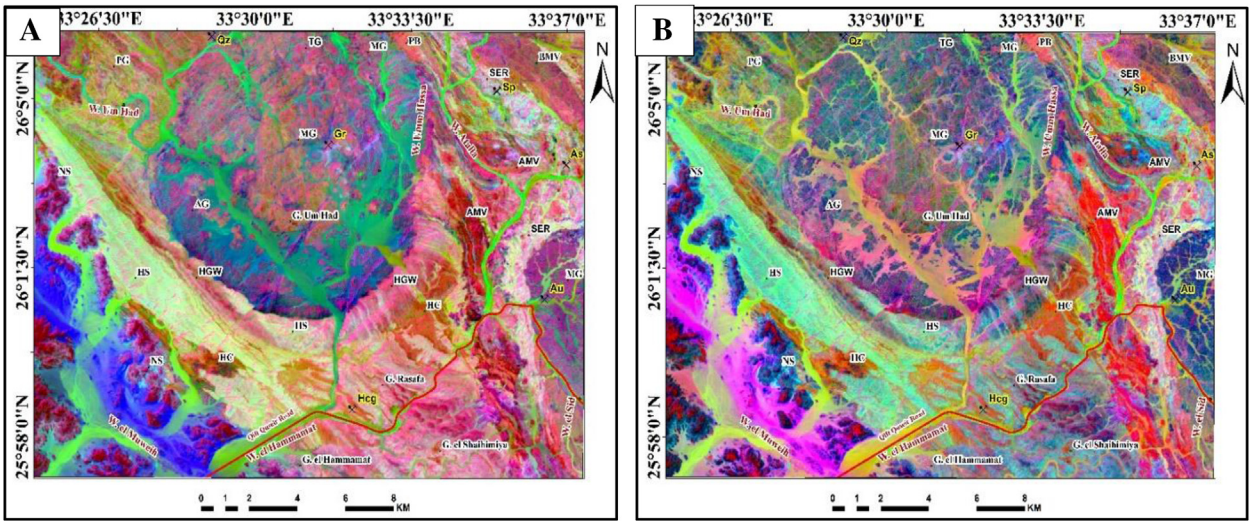


*Fig. 5. (a) Principal Component (PC) image (PC1, PC2, PC3) in RGB of OLI bands. (b) Principal Component (PC) image (PC5, PC2, PC3 in RGB) of OLI bands, symbols as (Fig. 3).*

that the best PCA (PC1, PC2, PC3), as it separates the different types of granites; tonalite-granodiorite in yellow green, monzogranite orange red, and alkali-granite as purple color, also, the acid, and basic metavolcanics in red and violet respectively. As well as the three types of Hammamat molasse sediments could be also differentiated (Fig. 5a). Moreover, the PCA (PC5, PC2, PC3) shows well differentiation of the rock units, where the psammitic gneiss and migmatites show olive drab, serpentinite as light blue, pillowed basalt into crimson, acid to intermediate metavolcanics with red color, basic to intermediate metavolcanics dark yellow slat blue color, Hammamat graywackes purple red color, Hammamat Conglomerate orange color, Hammamat silt with blue sky color, alkali granite with Claret violet color, monzogranite with indigo color (Fig. 5b).

### 3.2.4. *The minimum noise fraction (MNF)*

The Minimum Noise Fraction transform method is a data reduction procedure comprised of sequential processes. The first rotation decorrelates and rescales the noise in the data using the main components of the noise covariance matrix (a technique known as noise whitening), resulting in transformed data with unit variance and no band-to-band correlations. The second process takes the original correlation into account and creates a set of components containing weighted information about the variance in all bands of the dataset [33].

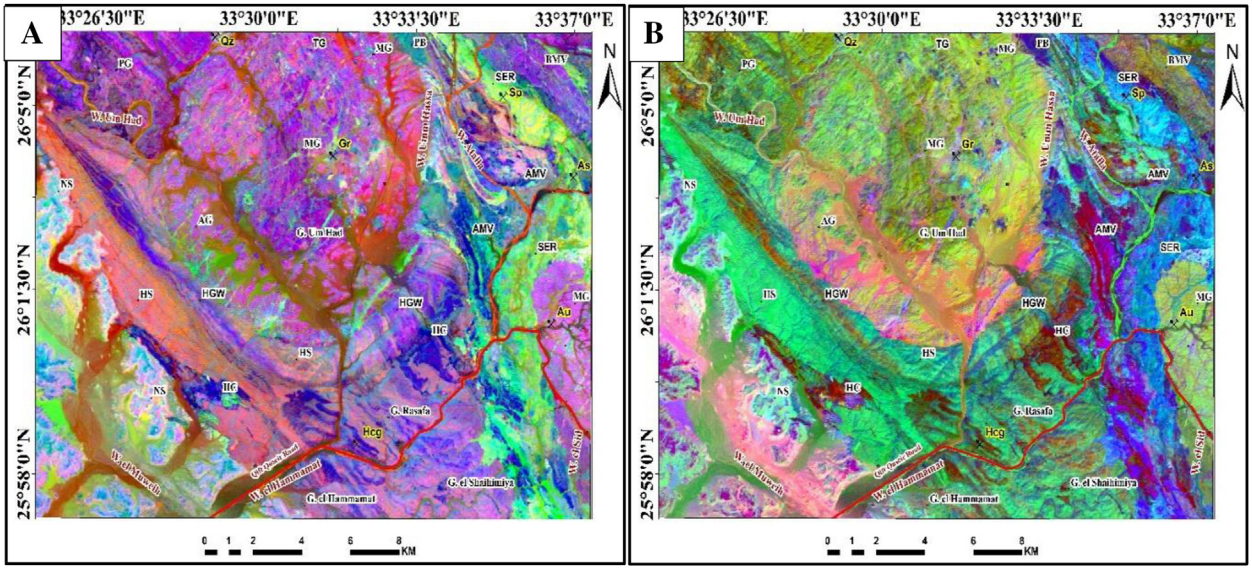


*Fig. 6. (a) Minimum Noise Fraction image (MNF5, MNF2, MNF3 in RGB) of OLI bands. (b) Minimum Noise Fraction image (MNF1, MNF2, MNF5 in RGB) of OLI bands, symbols as (Fig. 3).*

Also known as the Noise-Adjusted Principal Components (NAPC) transform [34]. The present study shows the best MNF results (MNF5, MNF2, MNF3), and (MNF1, MNF2, MNF5). The MNF1, MNF2, MNF5 shows serpentinite as cyan, pillowed basalt into blue, acid to intermediate metavolcanics with red color, basic to intermediate metavolcanics yellow green color, Hammamat graywackes and Hammamat Conglomerate dark red color, Hammamat silt with green color, alkali granite with violet color, monzogranite with lime green color (Fig. 6a). In the MNF5, MNF2 and MNF3, the serpentinite appeared as lime color, acid to intermediate metavolcanics with blue color, basic to intermediate metavolcanics dark violet color, Hammamat graywackes and Hammamat Conglomerate purple color, Hammamat silt with violet blue color, alkali granite with green color, monzogranite with purple violet color (Fig. 6b).

## 4. Results

As a result of the image processing verified by geological field observations, a new detailed modified geological map at scale 1:20 000 has been established for the study area (Fig. 7). As well as by the remote sensing image processing we can differentiate the Hammamat molasses into three definite varieties, as well verified in the field work. The field check and sampling of the rock varieties show the three members of the Hammamat sediments of Shihimiya Formation represented by Rasafa siltstone at the base, Um Had conglomerate in the middle and then Umm Hassa greywacke in the top. Due to the presence of chlorite and illite minerals in some parts Rasafa siltstone is described mainly as greenish gray color, they are crosscutting by veinlets and offshoots of quartz veins. Sometimes red color siltstone is dominant in the south due to the iron enriched siltstone (Fig. 8a & b). The Um Had conglomerates are angular to subrounded pebbles, consisting of fragments and particles derived from the older granitoids and metavolcanics (Fig. 8c & d). The Hammamat conglomerates lie in contact with the serpentinite at Bir Um Fawakhir area (Fig. 9a). Umm Hassa greywackes are moderate to poorly sorting grains of angular to subrounded lithics and fragments of quartz, volcanics, feldspars and calcite, in Wadi Um Had area they are intruded by the Um Had granite (Fig. 9b & c).

## 5. Discussion and conclusion

This study integrated the satellite data and field investigation to establish a detailed remote sensing data based on a modified geological map at scale 1:20 000. Where the Hammamat sediments could be classified into the 3 known members of siltstone, conglomerate and graywackes, comparable with [27,28] and rather than the EGSMA 2000 [35]. The new map shows the different rock units; from the oldest to the youngest psammitic gneiss and migmatites located in northwest of Um Had area, dismembered ophiolitic rocks (pillowed basalt and serpentinite) in the eastern part along Wadi Atalla and Bir Um Fawakhir, metavolcanics (acid to intermediate and basic to intermediate metavolcanics) pervade Wadi Atalla, tonalite-granodiorite located in the central upper part of Um Had area in contact with Um Had granite and at the southern part of Bir Um Fawakhir area, Hammamat molasse sediments widespread in the study area, molasse sediments in this study are related to Shihimiya Formation and subdivided into three types, Hammamat silt (Rasafa siltstone), Hammamat conglomerate (Um Had conglomerate) and Hammamat graywackes (Um Hassa graywacke), younger granitoids (alkali granite and monzogranite), alkali granite located in the Bir Um Fawakhir in contact with Hammamat molasse sediments in the entrance of Um Had area, monzogranite located in the center of Um Had area, and the Nubia sandstone located in the western part of Wadi Hammamat area.

According to the OIF ranking of Landsat-8, the best FCC for lithological discrimination especially the plutonic and volcanic rocks are 7,6,1, 7,6,2, and 751. The appropriate band ratios used to separate rock boundaries are 6/7, 6/5 and 4/2 after [30]. Moreover, the new band ratio (7/5, 5/3&3/1) enabled us differentiation between the three Hammamat molasse types as mentioned before. As well as the MNF5, MNF2, MNF3, and MNF1, MNF2, MNF5 gave the best results of MNF methods. Moreover, the best PCA {(PC1, PC2and PC3) and (PC5, PC2and PC3)} which gave details about the structure and rock boundaries of the study area.

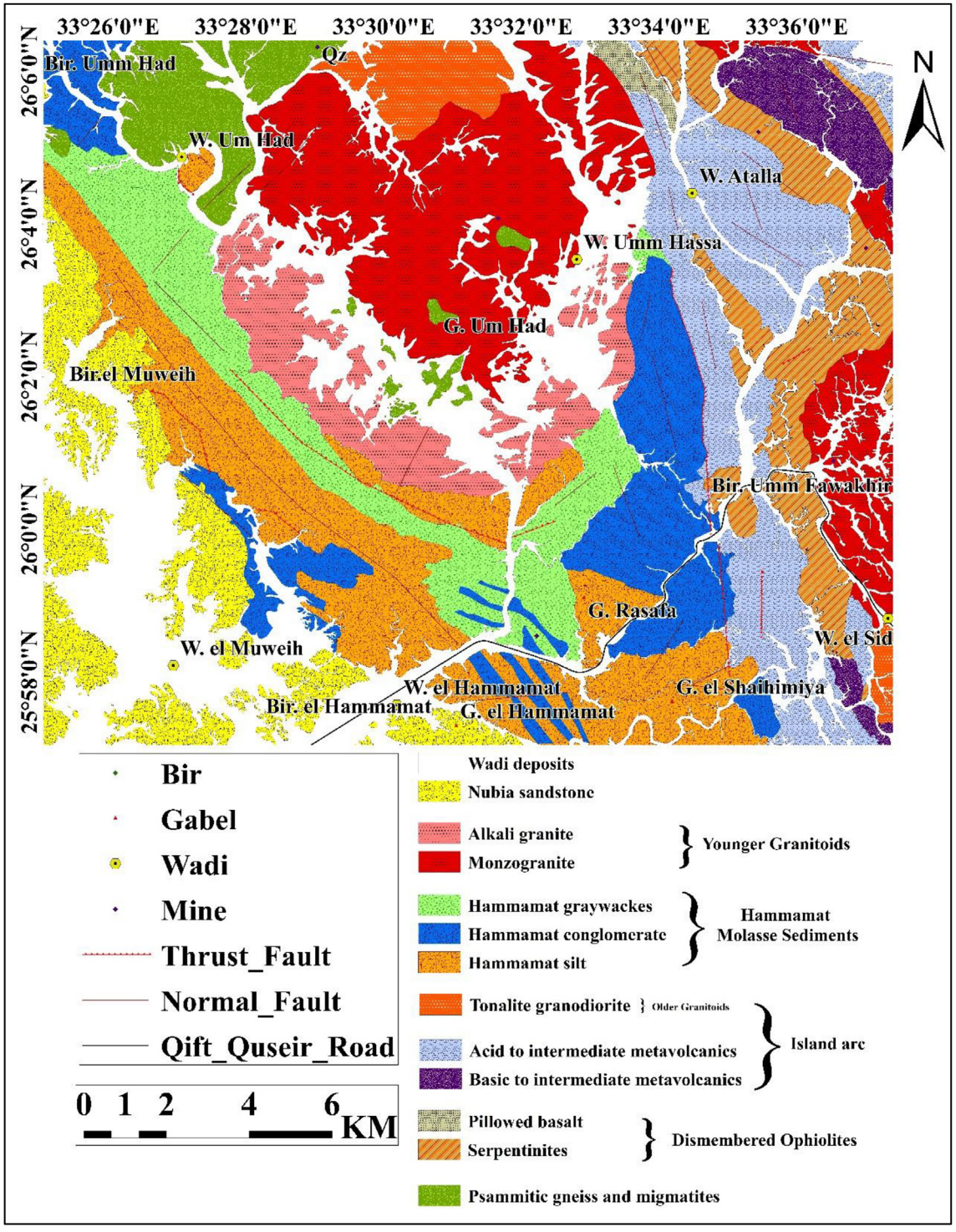


*Fig. 7. Geological map of the study area.*

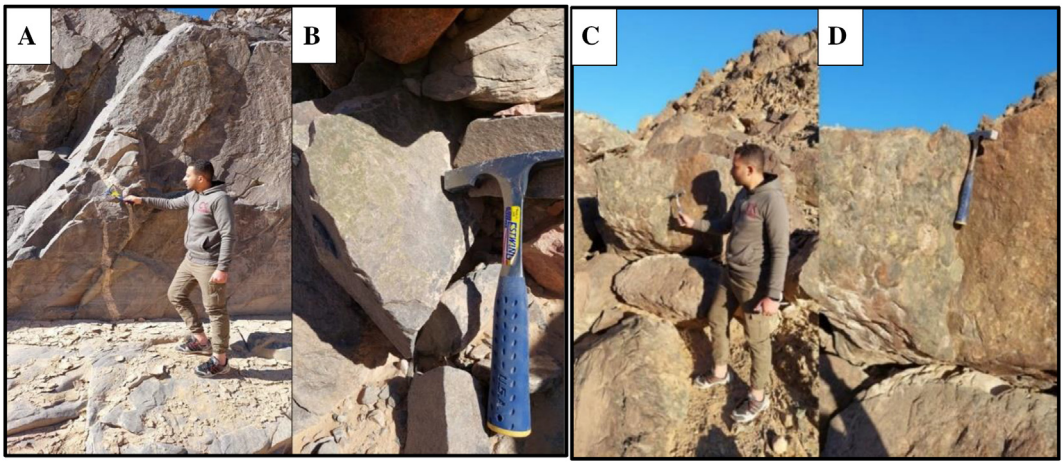


*Fig. 8. (a) Hammamat siltstone invaded by quartz veins. (B) Greenish color of Hammamat siltstone due to presence of chloride. (c, d) Um Had conglomerate represented by angular to subrounded pebbles.*

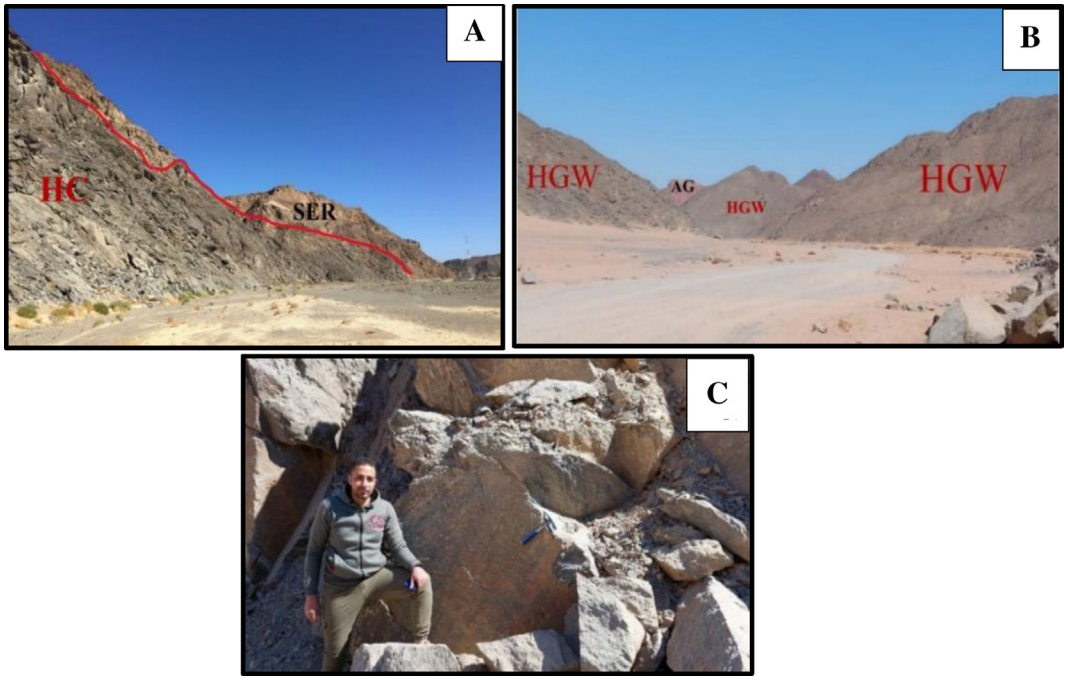


*Fig. 9. (a) Sharp contact between Hammamat conglomerate (HC) and serpentinite (SER) of Bir Um Fawakhir area. (b) contact between Umm Hassa graywacke (HGW) and Um Had granite (AG) in the entrances of Wadi Um Had area. (c) This figure shows Um Had Graywacke.*

Finally, the geological mapping is one of the most important strengths of remote sensing combining with field work and analytical techniques.

## Conflicts of interest

There are no conflicts of interest regarding this research.

## References

[1] Kennedy WQ. The structural differenciation of Africa in the Pan-African (+/-500 my) tectonic episode. University of Leeds, Research Institute of African Geology, Annual Report on Scientific Results. Int J Geosci 1964:48–9.
[2] Kröner A. Pan African plate tectonics and its repercussions on the crust of Northeast Africa. Geol Rundsch 1979;68: 565–83.

[3] El-Gaby S, El-Nady O, Khudeir A. Tectonic evolution of the basement complex in the central Eastern Desert of Egypt. Geol Rundsch 1984;73:1019−36.
[4] Abdeen MM, Greiling RO. A quantitative structural study of late Pan-African compressional deformation in the Central Eastern Desert (Egypt) during Gondwana assembly. Gondwana Res 2005;8:457−71.
[5] Johnson PR, Andresen A, Collins AS, Fowler AR, Fritz H, Ghebreab W, et al. Late Cryogenian−Ediacaran history of the Arabian−Nubian Shield: a review of depositional, plutonic, structural, and tectonic events in the closing stages of the northern East African Orogen. J Afr Earth Sci 2011;61:167−232.
[6] Abd El-Rahman Y, Polat A, Dilek Y, Kusky TM, El-Sharkawi M, Said A. Cryogenian ophiolite tectonics and metallogeny of the central Eastern Desert of Egypt. Int Geol Rev 2012;54:1870−84.
[7] Hume WF, Lyons HG. Geology of Egypt: the fundamental pre-cambrian rocks of Egypt and the Sudan; their distribution, age, and character. The metamorphic rocks. Government Press; 1934.
[8] Schürmann HME. Pre-Cambrian of the gulf of suez area. Éditeur non identifié 1953;1:115−35.
[9] Schürmann HME. The pre-cambrian along the guld of suez and the norther part of the red sea. Brill Archive 1966;3: 30−40.
[10] El Shazly EM. The classification of the precambrian and other rocks of magmatic affiliation in Egypt. India: UAR International Geol. Congress; 1964.
[11] Akaad MK, Noweir AM. Lithostratigraphy of the hammamat−um Seleimat district, Eastern Desert, Egypt. Nature 1969;223:284−5.
[12] El Ramly MF. A new geological map for the basement rocks in the Eastern and Southwestern desert of Egypt: scale 1: 1,000,000. Annals of the Geological Survey of Egypt; 1972.
[13] Ries AC, Shackleton RM, Graham RH, Fitches WR. Pan-African structures, ophiolites and mélange in the Eastem Desert of Egypt: a traverse at 26 N. The Geological Society of London 1983;140:75−95.
[14] El-Gaby S, List FK, Tehrani R. Geology, evolution and metallogenesis of the Pan-African belt in Egypt. the Pan-African belt of Northeast Africa and adjacent areas: tectonic evolution and economic aspects of a late proterozoic Oregon, Braunschweig. 1988. p. 17−68.
[15] Abdel-Khalek ML, Takla MA, Sehim A, Hamimi Z, el Manawi AW. Geology and tectonic evolution of Wadi Beitan area, southeastern Desert, Egypt. International Conference on Geology of the Arab World; Dar Al-Madina Al-Monawara press, Cairo, Egypt. 1992. p. 369−94.
[16] Ragab AI, el Alfy Z. Arc-arc collision model and its implications on a proposed classification of the Pan-African rocks of the Eastern Desert of Egypt. MERC Ain Shams University of Earth Science Series 1996;10:89−101.
[17] El Gaby S, List FK, Tehrani R. The basement complex of the Eastern Desert and sinai. Routledge: The Geology of Egypt; Routledge, London. 2017. p. 175−84.
[18] El-Fadly MA, Hamid S, Abu-Elrus MA, Khudeir AA. An inquiry into the structural evolution of the Neoproterozoic Shait granite complex, South Eastern Desert, Egypt. J Geol, Assiut University 2018;47:1−16.
[19] El-Gaby S, Khudeir AA, Tawabi MA, Atalla RF. The metamorphosed volcano-sedimentary succession of Wadi Kid, southeastern Sinai, Egypt. 1991.
[20] Gahlan HA, Azer MK, Khalil AES. The neoproterozoic Abu Dahr ophiolite, South Eastern Desert, Egypt: petrological characteristics and tectonomagmatic evolution. Mineral Petrol 2015;109:611−30.
[21] Sultan M, Arvidson RE, Sturchio NC. Mapping of serpentinites in the Eastern Desert of Egypt by using Landsat thematic mapper data. Geology 1986;14:995−9.
[22] `Sultan M, Arvidson R, Sturchio NC. Digital mapping of ophiolite melange zones from Landsat Thematic Mapper TM data in arid areas: meatiq dome, Egypt. Geological Society of America Annual Meeting, Abstracts with Programs 1986;18:766.
[23] Amer R, Kusky T, Reinert PC, Ghulam A. Image processing and analysis using Landsat ETM+ imagery for lithological mapping at Fawakhir, Central eastern desert of Egypt. Baltimore, Maryland: ASPRS 2009 Annual Conference; 2009.
[24] Kamel M, Youssef M, Hassan M, Bagash F. Utilization of ETM+ Landsat data in geologic mapping of wadi ghadir-gabal zabara area, central Eastern Desert, Egypt. The Egyptian J Remote Sensing and Space Sci 2016;19:343−60.
[25] Kamel M, Abdeen MM, Youssef MM, Orabi AM, Abdelbaky E. Utilization of landsat-8 (OLI) image data for geological mapping of the neo-proterozoic basement rocks in the central Eastern Desert of Egypt. J Indian Society of Remote Sensing 2022;50:469−92.
[26] Hassan SM, Sadek MF. Geological mapping and spectral based classification of basement rocks using remote sensing data analysis: the Korbiai-Gerf nappe complex, South Eastern Desert, Egypt. J Afr Earth Sci 2017;134:404−18.
[27] Hamimi Z, Hagag W, Kamh S, El-Araby A. Application of remote-sensing techniques in geological and structural mapping of Atalla shear zone and environs, central Eastern Desert, Egypt. Arabian J Geosci 2020;13:1−27.
[28] El-Wahed A, Mohamed A. The role of the najd fault System in the tectonic evolution of the Hammamat molasse sediments, Eastern Desert, Egypt. Arabian J Geosci 2010;3:1−26.
[29] Akaad MK, Noweir AM. Geology and lithostratigraphy of the Arabian desert orogenic belt of Egypt between latitudes 25° 35'and 26° 30'N. Precambrian Res 1978;6:A6.
[30] Zoheir B, Emam A, Abdel-Wahed M, Soliman N. Multispectral and radar data for the setting of gold mineralization in the South Eastern Desert, Egypt. Rem Sens 2019;11:1450.
[31] Sabins FF. Remote sensing for mineral exploration. Ore Geol Rev 1999;14:157−83.
[32] Jensen JR. Introductory digital image processing: a remote sensing perspective. Prentice-Hall Inc; New Jersey, US. 1996.
[33] Green AA, Berman M, Switzer P, Craig MD. A transformation for ordering multispectral data in terms of image quality with implications for noise removal. IEEE Trans Geosci Rem Sens 1988;26:65−74.
[34] Lee JB, Woodyatt AS, Berman M. Enhancement of high spectral resolution remote-sensing data by a noise-adjusted principal components transform. IEEE Trans Geosci Rem Sens 1990;28:295−304.
[35] Amer R, Kusky T, Ghulam A. Lithological mapping in the central Eastern Desert of Egypt using ASTER data. J Afr Earth Sci 2010;56:75−82.